

The binary millisecond pulsar PSR J1023+0038 – II. Optical spectroscopy

T. Shahbaz,^{1,2}★ M. Linares,^{3,4} P. Rodríguez-Gil^{1,2}, J. Casares^{1,2}

¹*Instituto de Astrofísica de Canarias (IAC), E-38205 La Laguna, Tenerife, Spain*

²*Departamento de Astrofísica, Universidad de La Laguna (ULL), E-38206 La Laguna, Tenerife, Spain*

³*Department de Física, EEBE, Universitat Politècnica de Catalunya, c/ Eduard Maristany 10, 08019 Barcelona, Spain*

⁴*Institute of Space Studies of Catalonia (IEEC), E-08034 Barcelona, Spain*

12th June 2019

ABSTRACT

We present time-resolved optical spectroscopy of the “redback” binary millisecond pulsar system PSR J1023+0038 during both its radio pulsar (2009) and accretion disc states (2014 and 2016). We provide observational evidence for the companion star being heated during the disc-state. We observe a spectral type change along the orbit, from \sim G5 to \sim F6 at the secondary star’s superior and inferior conjunction, respectively, and find that the corresponding irradiating luminosity can be powered by the high energy accretion luminosity or the spin down luminosity of the neutron star. We determine the secondary star’s radial velocity semi-amplitude from the metallic (primarily Fe and Ca) and H α absorption lines during these different states. The metallic and H α radial velocity semi-amplitude determined from the 2009 pulsar-state observations allows us to constrain the secondary star’s true radial velocity $K_2=276.3\pm 5.6$ km s⁻¹ and the binary mass ratio $q=0.137\pm 0.003$. By comparing the observed metallic and H α absorption-line radial velocity semi-amplitudes with model predictions, we can explain the observed semi-amplitude changes during the pulsar-state and during the pulsar/disc-state transition as being due to different amounts of heating and the presence of an accretion disc, respectively.

Key words: binaries: close – stars: fundamental parameters – stars: individual: PSR J1023+0038 – stars: neutron – X-rays: binaries

1 INTRODUCTION

Radio millisecond pulsars (MSP) are fast rotating magnetic neutron stars, that were spun up via the transfer of angular momentum from the companion star to the neutron star in a low mass X-ray binary (LMXB) (Alpar et al. 1982; Radhakrishnan & Srinivasan 1982). With the discovery of the first “transitional” MSP (tMSP) PSR J1023+0038 (Archibald et al. 2009), the connection between rotation-powered MSPs and accretion-powered LMXBs was established. The MSPs M28I (Papitto et al. 2013) and XSS J12270–4859 (Bassa et al. 2014) have also switched back and forth between a rotation-powered radio pulsar state (“pulsar-state”) and an accretion-powered state which shows X-ray pulsations and accretion disc signatures (“disc-state”).

PSR J1023+0038 was discovered by Bond et al. (2002) as part of the “Faint Images of the Radio Sky at Twenty Centimeters” (FIRST) survey. It was initially classified as a cataclysmic variable in 2001 because the optical counterpart to the radio source displayed short time-scale flickering and a blue optical spectrum with double-

peaked emission lines, associated with an accretion disc (Szkody 2003). Optical photometry taken in 2003 (Woudt et al. 2004) and 2004 (Homer et al. 2006) did not show the rapid, large flickering events seen in the 2001 light curve, suggesting that the system had changed state. Only a repetitive 4.75476(2) h single-humped modulation was observed (Woudt et al. 2004). Indeed Thorstensen & Armstrong (2005) confirmed this state transition because the optical spectrum taken in 2003 was dominated by strong absorption features and lacked the prominent emission lines observed in the 2001 spectrum. They performed a time-resolved optical spectroscopic and photometric study of PSR J1023+0038, in the what we know now to be the “pulsar-state”. They found the companion star to be a late-type G5 star with an absorption-line radial velocity semi-amplitude 268 ± 3 km s⁻¹ modulated on an orbital period $P_{\text{orb}}=4.754$ h. The optical light curves taken in 2004 revealed a single-humped modulation, explained in terms of an X-ray heated companion star in a system with an orbital inclination angle of $i \sim 55^\circ$. Combining the photometric and radial velocity studies led to the conclusion that the system was not a cataclysmic variable with a white dwarf, but instead an X-ray binary harbouring a neutron star. Indeed, the X-ray binary scenario also explained the 2004 X-ray observations which

★ E-mail: tsh@iac.es

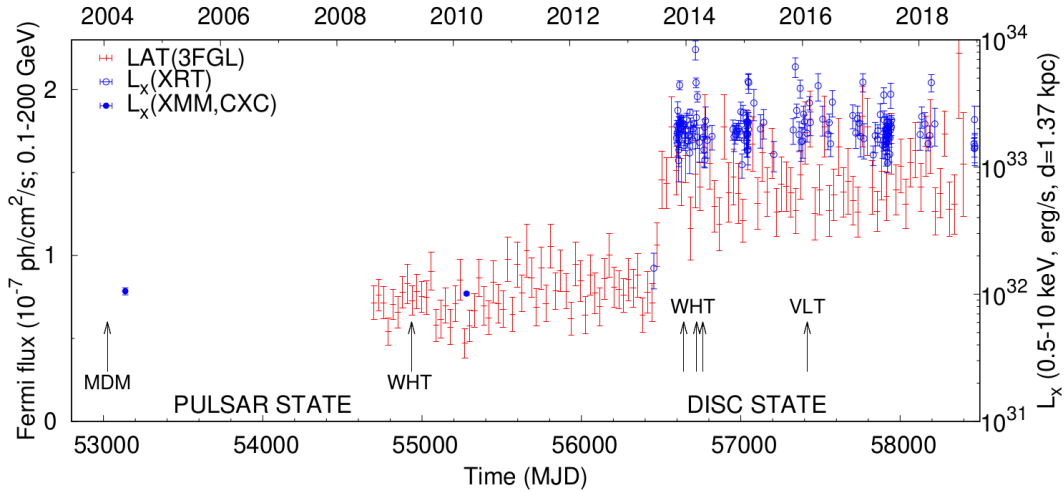


Figure 1. The Fermi LAT light curve is shown with red symbols (photon flux in the 0.1–200 GeV band; from the LAT 3FGL catalogue (https://fermi.gsfc.nasa.gov/ssc/data/access/lat/4yr_catalog/ap_lcs.php)). The state transition is clearly visible in mid 2013. We also show the 0.5–10 keV X-ray luminosities from Swift-XRT data (open blue circles), as well as the X-ray luminosities measured with *Chandra* (Bogdanov et al. 2011) and *XMM-Newton* (Homer et al. 2006) before 2013 (filled blue circles). The distance is taken from the known radio parallax (Deller et al. 2012). The arrows show the time of the MDM 2004 (Thorstensen & Armstrong 2005), WHT ISIS 2009, WHT ISIS 2014 and VLT X-SHOOTER 2016 optical observations.

were dominated by a hard X-ray power-law component (Homer et al. 2006).

In 2007 the system was detected as a radio pulsar with a spin period of 1.69 ms (Archibald et al. 2009), confirming that the primary was indeed a neutron star and that PSR J1023+0038 is a low-mass X-ray binary. This was the first direct evidence of an MSP in a binary system transitioning between two distinct states, and gave significant support to the “recycled” scenario for the origin of MSPs. Between 2008 and 2012 PSR J1023+0038 was consistently observed as an eclipsing radio millisecond pulsar, where the radio eclipses are attributed to ionized material being forced off the companion star by the pulsar wind, as seen in other similar MSPs called “black-widows” (Fruchter et al. 1988).

In 2013 June, after about 10 years in the pulsar-state, PSR J1023+0038 transitioned back to the disc-state, as witnessed by the increased X-ray and gamma-ray flux (Fig. 1) and the disappearance of radio pulsations. PSR J1023+0038 was detected as a radio pulsar in 2013 June 15, but eight days later it was not detected in the radio (Stappers et al. 2014). After the transition, the system brightened by ~ 1 mag in the optical and showed several broad double-peaked emission lines (Halpern et al. 2013; Linares et al. 2014). There was also a disappearance of radio pulsations and an increase in the X-ray and gamma-ray luminosities by a factor of ~ 20 and ~ 10 , respectively (Linares 2014; Takata et al. 2014; Stappers et al. 2014; Patruno et al. 2014). All these factors provided compelling evidence that an accretion disc had re-formed, indicating that PSR J1023+0038 had switched back from a radio millisecond pulsar (pulsar-state) to a low-mass X-ray binary (disc-state).

In Shahbaz et al. (2015, paper I) we presented the results of our optical photometric campaign, which revealed unprecedented fast variability. Here we present the results of our optical spectroscopic campaign of PSR J1023+0038 in the disc-state, including those summarized in Linares et al. (2014), as well as archival optical spectroscopy taken during the pulsar-state. Previous spectroscopic studies do not cover full orbital cycles, have poor spectral resolution or do not compare the different states (Thorstensen & Armstrong 2005; Wang et al. 2009; Hakala & Kajava 2018). We perform a

spectral type, radial velocity curve analysis and compute Doppler maps of the $H\alpha$ emission-line in both the pulsar- and disc-state. Finally, we compare the radial velocity semi-amplitude with model predictions, which account for the effects of heating and an accretion disc.

2 OBSERVATIONS AND DATA REDUCTION

2.1 WHT observations

We observed PSR J1023+0038 between November 2013 and April 2014 with the William Herschel Telescope (WHT), at the Roque de los Muchachos Observatory on La Palma, in order to obtain low-resolution optical spectra of the system in the disc state (Linares et al. 2014). We used the double-armed Intermediate dispersion Spectrograph and Imaging System (ISIS) optical spectrometer with the R600B and the R600R gratings as well as the Auxiliary-port CAMera (ACAM) with the 400 lines/mm transmission volume phase holographic (VPH) grating. These observations were taken about 6 months after PSR J1023+0038 transitioned from the radio pulsar to the disc state around 2013 June 30 (Patruno et al. 2014; Stappers et al. 2014).

The images were first de-biased, and flat-fielded using standard procedures within IRAF¹. After subtracting the bias level, the images were divided by a median sky flat field that was normalised by fitting high order spline functions to remove the detector specific spectral response. The 1-D spectra were then extracted using optimal extraction (Horne 1986) as implemented in PAMELA (Marsh 1989), which is part of the STARLINK² software. The wavelength calibration was done using CuNe/CuAr arc lamp spectra taken before, after and between science spectra, extracted from the same region as the

¹ IRAF is distributed by the National Optical Astronomy Observatory, which is operated by the Association of Universities for Research in Astronomy, Inc., under cooperative agreement with the National Science Foundation. <http://iraf.noao.edu/>

² <http://starlink.eao.hawaii.edu/starlink>

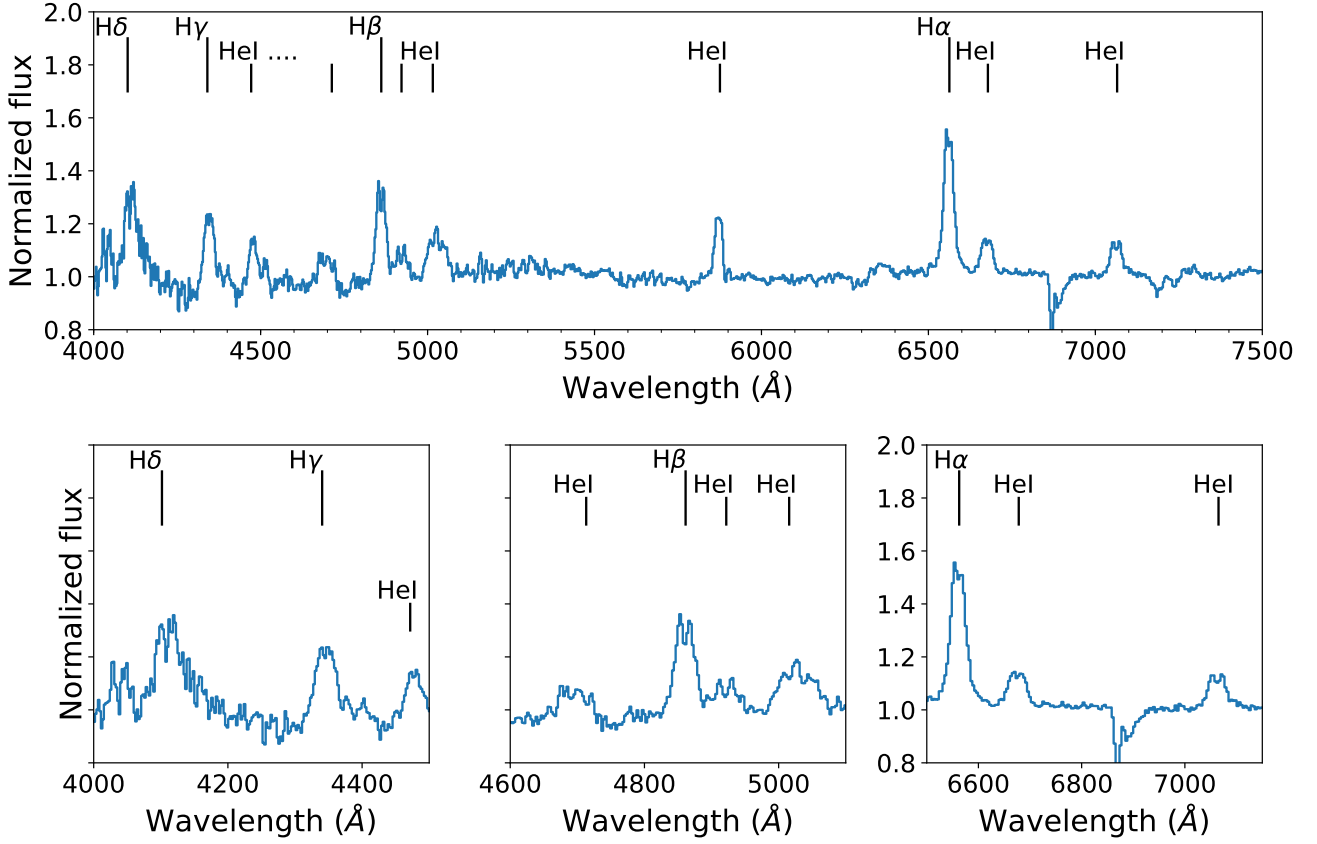


Figure 2. Normalized phase-averaged ACAM spectrum of PSR J1023+0038 in the disc-state. The main emission lines are identified (vertical lines).

Table 1. Summary of optical spectroscopic observations of PSR J1023+0038.

Telescope (diameter)	Instrument Configuration	Range (λ , Å)	Disp. (Å/pixel) FWHM Res. (km/s)	UT date start	UT time start–stop	Exposures	S/N per spectrum	Orbital phase	Airmass
— Observations presented in this paper —									
WHT (4.2-m)	ACAM V400+0.5"	3500–9400	3.4 350	2013-12-15	02:34–06:42	22×600 s	~11	0.88–1.75	1.13–1.73
WHT (4.2-m)	ISIS R600B+1.0"	B:3700–5300	0.88 100	2014-03-06	22:02–02:43	27×600 s	~11	0.84–1.82	1.13–1.43
	ISIS R600R+1.0"	R:5500–7200	0.98 70	2014-03-06	22:02–02:43	27×600 s	~19	0.84–1.82	1.13–1.43
WHT (4.2-m)	ACAM V400+0.5"	3500–9400	3.4 290	2014-04-14	20:15–01:05	28×600 s	~19	0.32–1.34	1.13–1.65
— Observations downloaded from archives —									
WHT (4.2-m)	ISIS H2400B+0.82"	B:4300–4700	0.22 20	2009-04-12	20:13–01:13	26×600 s	~3	0.53–1.50	1.07–1.62
	ISIS R1200R+0.82"	R:6200–6900	0.50 24	2009-04-12	20:13–01:13	26×600 s	~10	0.53–1.50	1.07–1.62
VLT (8.2-m)	X-SHOOTER ECHELLE+0.9"	VIS:5300–10200	0.2 40	2016-01-30	04:02–08:28	42×372 s	~50	0.12–1.97	1.11–1.36
	X-SHOOTER ECHELLE+0.9"	UBV:3000–5560	0.2 70	2016-01-30	04:02–08:28	42×372 s	~50	0.12–1.97	1.11–1.36

closest target spectrum in time. Sets of about 20 to 50 line centroid positions, depending on the instrument, were fitted with a 4–6 order polynomial to obtain the dispersion relation, which was interpolated linearly in time to account for instrumental flexure when calibrating the spectra. The wavelength calibration was subsequently checked and refined using the sky emission lines, which were also used to measure the spectral resolution (full width at half-maximum, FWHM, of the sky lines). The exposure time, wavelength range, dispersion and resolution are shown in Table 1.

2.2 Archival data

We downloaded the Isaac Newton Group archival data of PSR J1023+0038 carried out on 2009 April 12 with ISIS on the WHT (P.I. Jonker). ISIS was fitted with the H2400B and the R1200R gratings in the blue and red arm, respectively and a 0.82 arcsec slit width was used. The spectra were extracted using the same procedure as the WHT 2014 data. The exposure time, wavelength range, dispersion and resolution are shown in Table 1.

We also downloaded the ESO Very Large Telescope (VLT) archival data of PSR J1023+0038 taken on 2016 January 30 under programme 096.D-0808 (P.I. Bassa) with the X-SHOOTER medium resolution ($R=4000$ to 7000) spectrograph (Vernet & et al. 2011). A slit width of 1.0 arcsec in the UVB arm (2989–5560 Å) and 0.9 arcsec in the VIS arm (5337–10200 Å) and NIR arms (0.994–2.478 μm) was used. The UVB and VIS arm CCDs were binned by a factor of 2 and the exposure times were 360 s in the UVB arm, 372 s in the VIS arm and 400 s in the NIR arm. A total of 42 spectra were taken in nodding mode in each arm. The data reduction pipeline was used to optimally extract and calibrate the spectra (Freudling et al. 2013). The mean dispersion was 10 km s^{-1} and the spectral resolution measured from the sky lines was 40 km s^{-1} . In this paper we only use the UVB and VIS arm spectra, since no telluric stars were observed. The exposure time, wavelength range, dispersion and resolution are shown in Table 1.

3 AVERAGE SPECTRUM

In Fig. 2 we show the disc-state normalized phase-averaged WHT ACAM 2014 spectrum of PSR J1023+0038. Broad Balmer and He lines emission lines are clearly seen, which also show a double-horned profile related to the presence of an accretion disc.

4 ANALYSIS

In order to measure the absorption-line radial velocity curve and determine the spectral type of the companion star in PSR J1023+0038, we use cross-correlation and optimal subtraction techniques, respectively (see Marsh et al. 1994, for details). All analysis was performed with the MOLLY³ package. For a given template star we optimally subtract the variance-weighted Doppler-shifted target spectrum from the rotationally broadened template star spectrum. We perform a χ^2 test on the residuals of the subtraction, where the optimal value for the spectral type is obtained by minimizing χ^2 . Since both procedures require template star spectra, we compiled a library of high signal-to-noise A to K star template spectra with luminosity class V from the UVES Paranal Observatory Project (UVESPOP) archive (Bagnulo et al. 2003). We normalize the

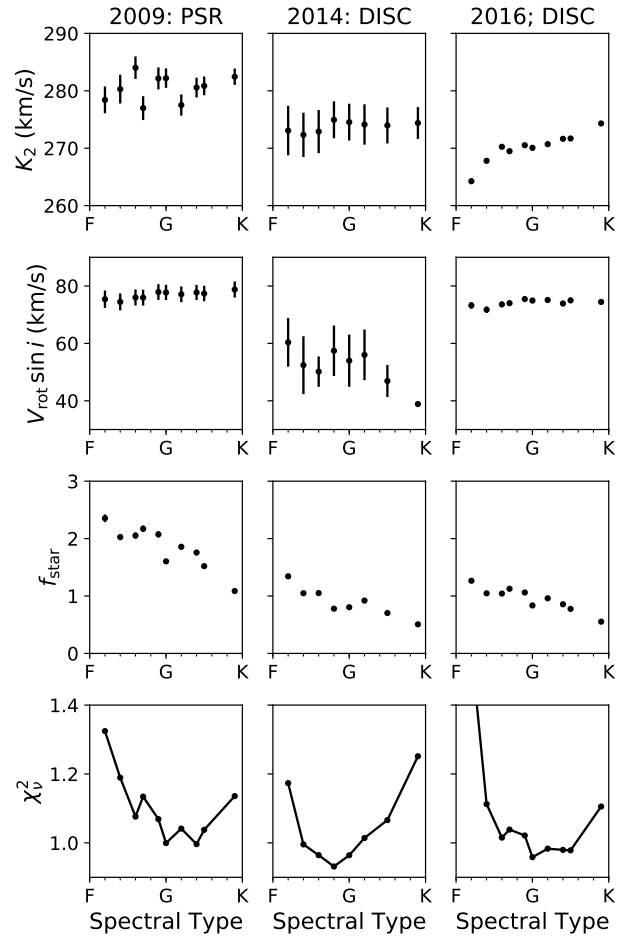


Figure 3. The cross-correlation radial velocity analysis and the optimal subtraction to determine the spectral type of the secondary star. The results are shown using all orbital phases. As a function of template star spectral type, we show the values of K_2 and determined from a circular orbit fit to the radial velocities, and the values for $v_{\text{rot}} \sin i$, f_{star} and χ^2 obtained from the optimal subtraction. The left, middle and right columns are the results for the ISIS 2009 (pulsar-state), ISIS 2014 (disc-state) and X-SHOOTER 2016 (disc-state) spectra, respectively.

spectra by determining a low-order spline fit to the continuum level and then divide the spectra by the fitted continuum. We degrade the template star spectra to match the same spectral resolution and heliocentric velocity scale as the target and interpolate all the spectra onto a logarithmic wavelength scale with the pixel size set by the target spectra.

4.1 Radial velocity curve

Firstly, we measure the projected orbital velocity of the companion star in PSR J1023+0038 by cross-correlating the spectra of the target with the template star of interest. We normalize the spectra similar as above and interpolate the spectra onto a logarithmic wavelength scale set by the target spectra. As the absorption lines in the target spectrum are rotationally broadened, the template star is broadened before performing the cross-correlation analysis, using the broadening estimated by McConnell et al. (2014). We use the wavelength

³ <http://deneb.astro.warwick.ac.uk/phsaap/software/>

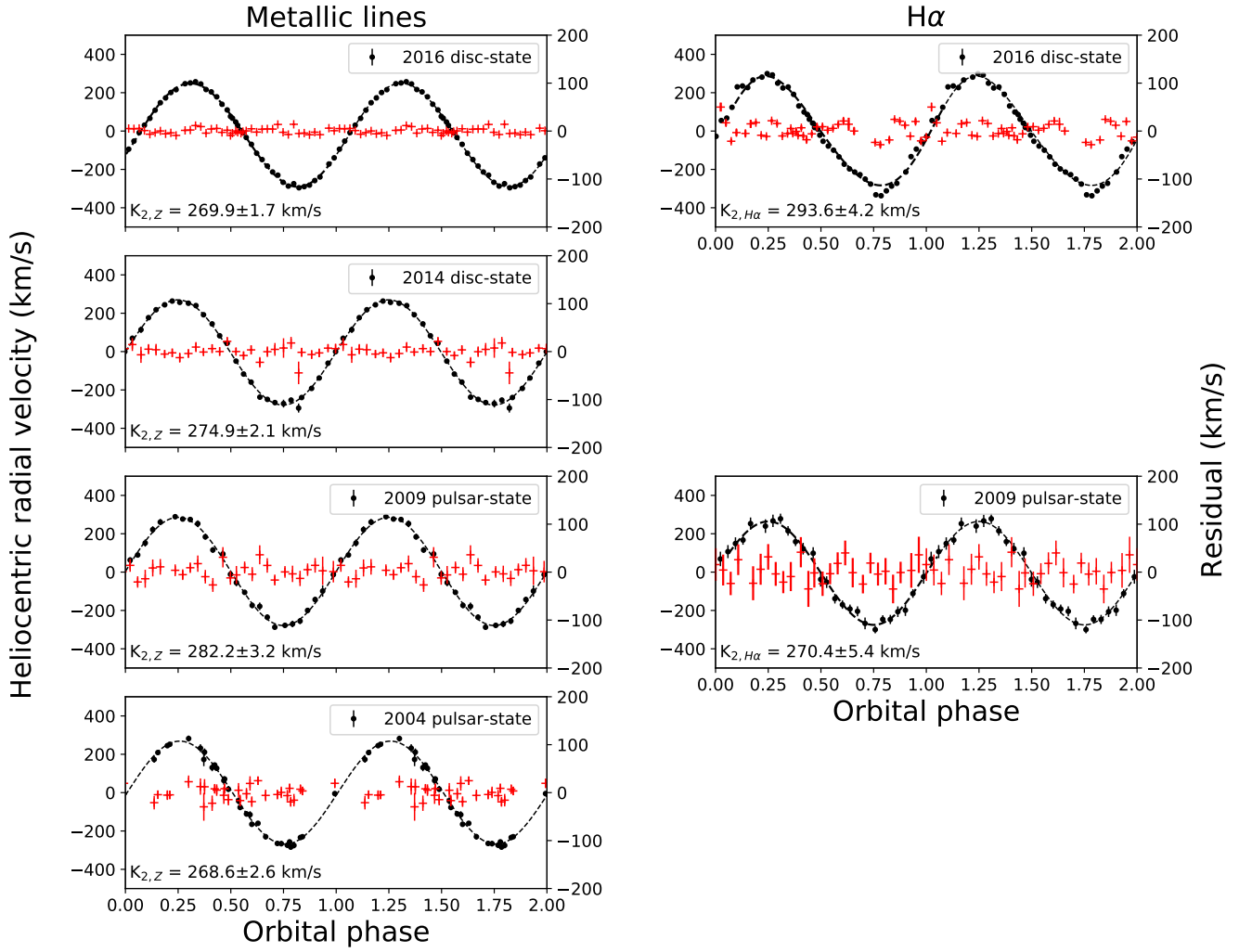


Figure 4. Left: The heliocentric radial-velocity curve (filled circles) of the secondary star in PSR J1023+0038, determined using the metallic (primarily Fe and Ca) lines. We show the 2004 pulsar-state (Thorstensen & Armstrong 2005), ISIS 2009 pulsar-state, ISIS 2014 disc-state and the X-SHOOTER 2016 disc-state radial velocities. Right: The heliocentric radial-velocity curve (filled circles) of the secondary star in PSR J1023+0038, determined using the residual H α absorption-line. We show the ISIS 2009 pulsar-state and the X-SHOOTER 2016 disc-state radial velocities. The solid line shows an eccentric orbit fit to the data and the red crosses show the residual after subtracting the fit. The data have been folded on the orbital ephemeris and are shown twice for clarity.

range 5500–6900 Å which contains numerous weak metallic absorption lines of Fe, Ca and Mg, excluding the H and He emission lines and interstellar features. We perform a least-squares fit of the radial velocities versus time using a circular orbit. The orbital period P_{orb} was fixed at the pulsar timing value $P_{\text{orb}}=0.1980963569(3)$ d (Archibald et al. 2013). T_0 was constrained to lie near the middle of the time span over which the observations were taken, and defines orbital phase 0 as inferior conjunction of the secondary star (see results in Table 2).

Thorstensen & Armstrong (2005) determine the radial velocities of PSR J1023+0038 in 2004 in the pulsar-state by cross-correlating spectra of PSR J1023+0038 with template stars. The wavelength range and spectral type template stars they use in the cross-correlation covers the wavelength range and template stars star used here. Here we use their radial velocities and perform the same least-squares fit as above.

4.2 Spectral type

Using the orbital parameters derived from the radial velocity fits above, we Doppler-correct and average the target spectra to the reference frame of the template star of interest, over a defined orbital phase range. In principle, the absorption features arising from the companion star should be relatively sharp because the Doppler shifts due to orbital motion have been corrected. However, the absorption lines are still broadened, due to the instrumental resolution of the spectrograph, the rotation of the secondary star and by changes in the orbital velocity during individual exposures. The broadening function that affects the target’s absorption lines consists of the convolution of the instrumental profile with the rotational broadening profile of the secondary star. There is also a further smearing due to the orbital velocity shift of the secondary star during a given exposure Δt at a given orbital phase, $\Delta V_{\text{smear}} \sim \left| \frac{\partial V_z}{\partial t} \right| \Delta t_\phi$. The orbital smearing is maximal at the conjunction phases and for an exposure

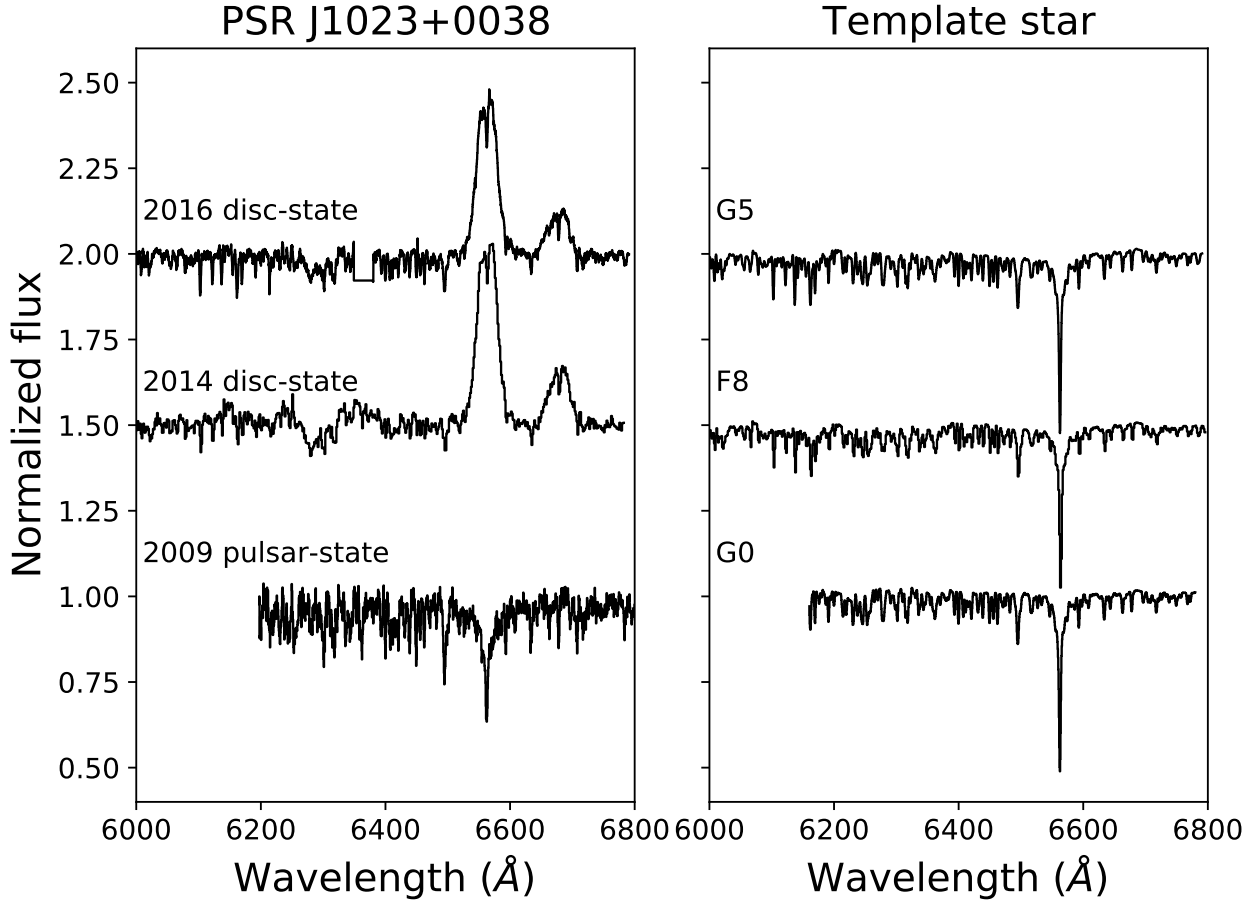


Figure 5. Left: the X-SHOOTER 2016 spectrum taken in the disc-state, the ISIS 2014 spectrum taken in the disc-state and the ISIS 2009 spectrum taken in the pulsar-state. (The gap in the X-SHOOTER 2016 data is due to an artifact in the reduction pipeline). Right: the corresponding optimally broadened template star spectrum. The spectra have been offset for clarity.

time of 600 s it is $\sim 60 \text{ km s}^{-1}$. Therefore, it is necessary to correct for smearing because the smearing is comparable to the rotational broadening (McConnell et al. 2014). For each target exposure, we first smear the template spectrum by convolution with a rectangular profile with an amount corresponding to the target’s radial velocity and exposure time, and then compute the average template star spectrum.

To determine the secondary star’s spectral type we compare a broadened version of the average, smeared template star spectrum with the target spectrum. We broaden the template star from 50 to 100 km s^{-1} by convolution with the Gray (1992) rotational profile. We subtract a constant, f_{star} , representing the fraction of light from the template star, multiplied by a smeared, rotationally broadened version of the template star. We eliminate long-scale trends in the residual spectrum by applying a high-pass Gaussian filter of $\text{FWHM}=400 \text{ km s}^{-1}$. We use a linear limb-darkening coefficient of 0.62 (Al-Naimiy 1978) appropriate for 6500 \AA and a mid-GV star. We perform a χ^2 test on the high-pass filtered residuals of the subtraction, where the optimal values of $v_{\text{rot}} \sin i$ and f_{star} were obtained by minimizing χ^2 . For the optimal subtraction procedure we use the wavelength range $6000\text{--}6900 \text{ \AA}$ which is common to

all data sets, excluding the emission lines. We also exclude the region $6250\text{--}6350 \text{ \AA}$ because it is contaminated by the weak Doppler smeared diffuse interstellar bands at 6283 \AA and the 6300 \AA [OI] sky emission-line.

5 RESULTS

5.1 Metallic absorption lines

In Fig. 3 we show the results using the ISIS 2009, ISIS 2014 and X-SHOOTER 2016 spectra of PSR J1023+0038 between orbital phase 0.0 and 1.0, for template stars in the F to K spectral range. The χ^2 versus spectral type obtained from the optimal subtraction has a minimum at $G2\pm 2$, $F8\pm 2$ and $G0\pm 2$ for the ISIS 2009 pulsar-state, ISIS 2014 disc-state and X-SHOOTER 2016 disc-state, respectively. The uncertainties in the spectral type were estimated from a parabolic fit to the minimum. For each data set, the result of an circular orbit fit to the radial velocities obtained using the optimal spectral type is shown in Table 2. For the optimal spectral type, we obtain metallic absorption-line radial velocity semi-amplitudes of $K_{2,Z}=282.2\pm 3.2 \text{ km s}^{-1}$, $274.9\pm 2.1 \text{ km s}^{-1}$ and $270.0\pm 1.7 \text{ km s}^{-1}$,

Table 2. Results of the fit to the radial velocity data using the metallic and H α absorption-line, taken at different epochs. Note that in each case, spectra between orbital phase 0.0 and 1.0 have been used.

Parameter	2004	2009	2014	2016
State	pulsar	pulsar	disc	disc
— Metallic absorption lines —				
γ (km s $^{-1}$)	0.1 \pm 2.7	3.5 \pm 3.0	-4.1 \pm 2.0	5.2 \pm 0.9
$K_{2,Z}$ (km s $^{-1}$)	268.6 \pm 3.5	282.2 \pm 3.2	274.9 \pm 2.1	270.0 \pm 1.7
T_0^a (d)	3025.0007 \pm 0.0005	4934.6491 \pm 0.0047	6723.0635 \pm 0.0027	7417.7871 \pm 0.00015
$v_{\text{rot}} \sin i$ (km s $^{-1}$)	-	77.7 \pm 2.7	-	74.9 \pm 0.9
f_{star}	-	1.6 \pm 0.5	0.78 \pm 0.3	0.84 \pm 0.01
Spectral Type	G5–G7 b	G0–G4	F6–G0	F8–G2
— H α absorption-line —				
$\delta\phi$ (km s $^{-1}$)	-	0.08 \pm 0.01	-	0.019 \pm 0.008
γ (km s $^{-1}$)	-	-5.5 \pm 4.6	-	-14.8 \pm 3.0
$K_{2,H\alpha}$ (km s $^{-1}$)	-	270.4 \pm 5.4	-	293.6 \pm 4.2
e	-	0.02 \pm 0.01	-	0.08 \pm 0.02

^a HJD 2450000+

^b Taken from [Thorstensen & Armstrong \(2005\)](#).

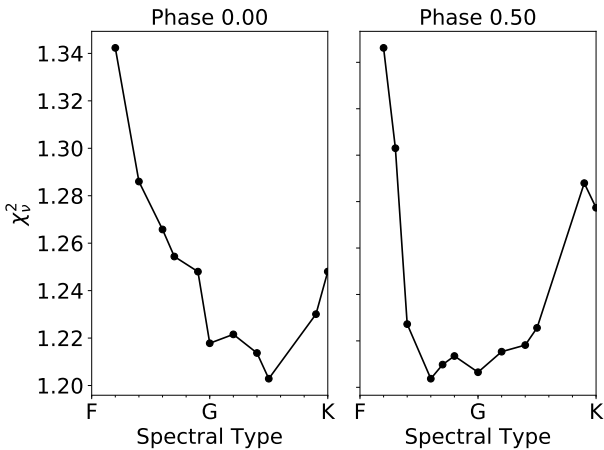


Figure 6. The results of the optimal subtraction to determine the spectral type of the secondary star using spectra taken around phase 0.0 and 0.5. We find the spectral type to be \sim G5 and \sim F5, around phase 0.0 and 0.5, respectively.

respectively. The 1σ errors are quoted where the error bars have been rescaled so that the reduced χ^2 of the optimal subtraction fit is 1. Fig. 4 (left) we show the radial velocity curves obtained from the ISIS 2009, ISIS 2014 and X-SHOOTER 2016 spectra folded on the ephemeris determined from the optimal spectral type. The value for T_0 determined independently for each dataset is consistent with the calculated T_0 adopting an ephemeris with constant orbital period.

To determine the secondary star’s rotational broadening the spectral resolution of the data should be less than the combined effects of the instrumental resolution plus orbital smearing. The ISIS 2014 spectra has the worst resolution and hence cannot be used to determine the secondary star’s rotational broadening. The

instrumental spectral resolution is 24, 70 and 40 km s $^{-1}$ for the ISIS 2009, 2014 and X-SHOOTER 2016 spectra, respectively. The maximum smearing is \sim 60 km s $^{-1}$ for the ISIS 2009 and 2014 spectra, and \sim 35 km s $^{-1}$ for the X-SHOOTER 2016 spectra. For the ISIS 2009 and X-SHOOTER 2016 spectra we obtain a $v_{\text{rot}} \sin i$ of 77.7 \pm 2.7 km s $^{-1}$ and 74.9 \pm 0.9 km s $^{-1}$, respectively. The 1σ errors are quoted where the error bars have been rescaled so that the reduced χ^2 of the optimal subtraction fit is 1. However, the ISIS 2014 data with the worst resolution, cannot resolve the star’s rotational broadening and hence the $v_{\text{rot}} \sin i$ we obtain is biased towards the blended lines. In Fig. 5 we show the Doppler-averaged spectrum of the ISIS 2004, ISIS 2009 and X-SHOOTER 2016 data taken as well as the optimal rotationally broadened template star for each data set. As one can see, the ISIS 2009 spectrum shows deeper absorption lines compared to the template star, indeed for any spectral type f_{star} is greater than 1, suggesting that the secondary star is peculiar (see Section 7).

5.2 Effects of irradiation

Although the binary has a circular orbit, the observed radial-velocity curve of the secondary star can appear non-circular. Heating effects can distort the radial-velocity curve leading to an apparent eccentric orbit ([Davey & Smith 1992](#); [Shahbaz et al. 2000](#)). We therefore fit the X-SHOOTER 2016 radial-velocity curve with an eccentric orbit to determine the effects of heating. We perform a least-squares fit of the radial velocities versus time using an eccentric orbit of the form,

$$V_2 = \gamma + K_2[\cos(\theta + \omega) + e \cos \omega], \quad (1)$$

where γ is the systemic velocity of the binary, θ is the true anomaly that varies with time, e is the eccentricity of the orbit, ω is the periastron angle and K_2 is the radial velocity semi-amplitude ([Iglesias-Marzoa et al. 2015](#)). The value for $\theta(t)$ is

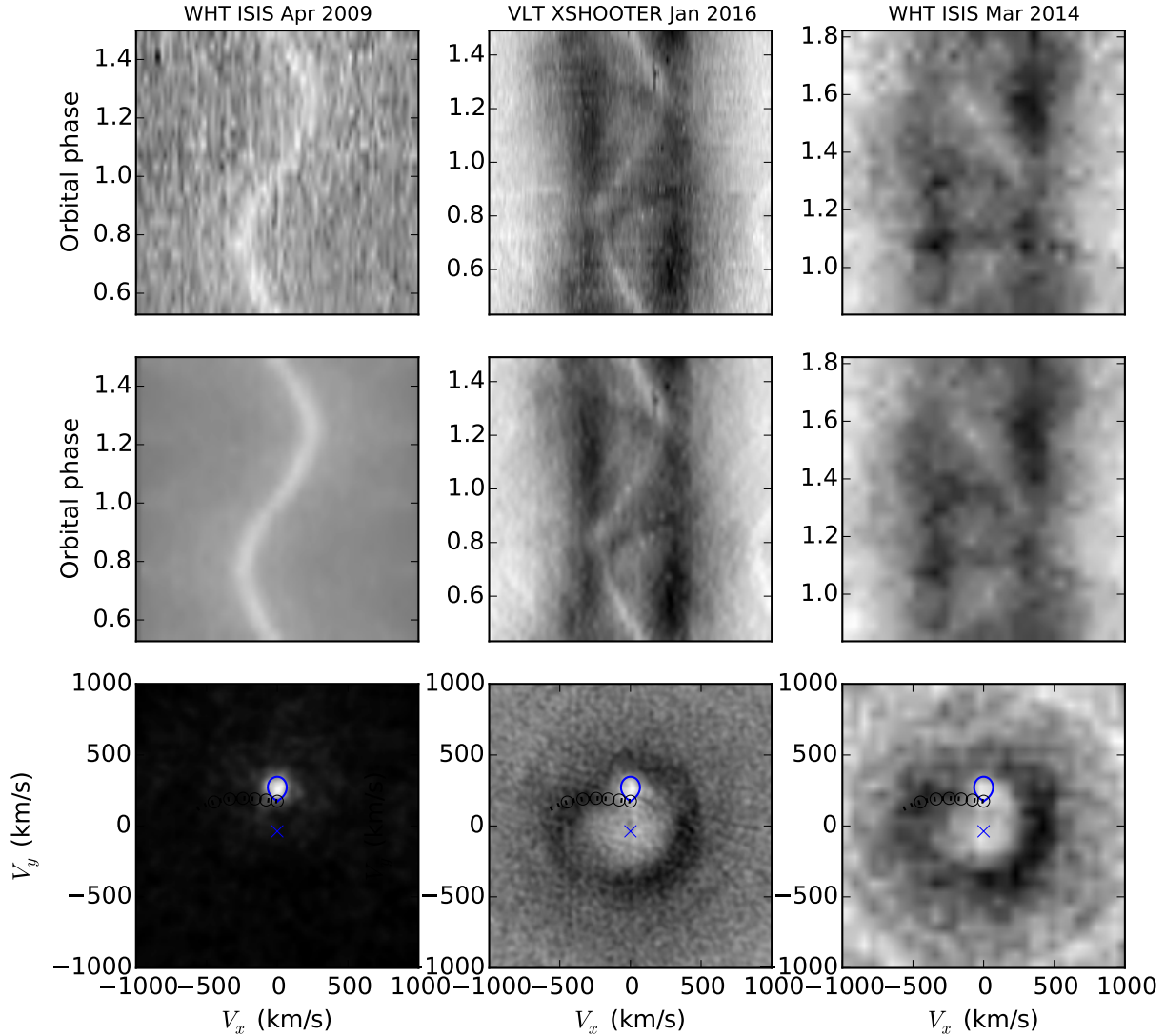


Figure 7. Trailed spectra and Doppler maps of the $H\alpha$ emission-line at different epochs. From left to right, WHT ISIS 2009, VLT X-SHOOTER 2016 and WHT ISIS 2014. From top to bottom; trailed spectra, computed spectra and Doppler maps. White and black show absorption and emission, respectively. The ISIS 2009 pulsar-state spectra clearly show the narrow $H\alpha$ absorption-line from the secondary star (white S-wave), which can also be seen in the VLT X-SHOOTER 2016 and WHT ISIS 2014 disc-state spectra. The Roche lobe of the secondary star is also plotted for $q=0.141$ and $K_2=270 \text{ km s}^{-1}$. The circles show the gas stream and the blue cross, the position of the neutron star.

given by $\tan[\theta(t)/2] = \sqrt{\frac{1+e}{1-e}} \tan(E/2)$, where E is the eccentric anomaly, obtained by numerically solving the Kepler equation $E - e \sin E = \frac{2\pi}{P} (t - T_0)$, where T_0 is the time of periastron passage and P_{orb} is the orbital period of the system. For the X-SHOOTER 2016 spectra, the G0 template star gives a fit with $e=0.017 \pm 0.002$, which is significantly better than a circular orbit at the 99.4 per cent level.

To see if the spectral type and thus effective temperature is different on the heated and non-heated hemisphere of the secondary star, we repeat the spectra type determination analysis in Section 4 by averaging the target spectra around orbital phase $\phi=0.00 \pm 0.15$ and orbital phase $\phi=0.50 \pm 0.15$. For the X-SHOOTER 2016 spectra, with high signal-to-noise, we find that the secondary star's spectral

type around phase 0.0 and 0.5 is significantly different, $\sim G5$ and $\sim F6$, respectively (see Fig. 6).

5.3 $H\alpha$ absorption-line

A trailed spectrogram of the ISIS 2009 pulsar-state data clearly shows narrow $H\alpha$ in absorption (see Fig. 7), which arises from the secondary star. For the disc-state spectra, the accretion double-peaked emission-line profile contaminates the narrow $H\alpha$ absorption-line. Despite this, narrow $H\alpha$ absorption is clearly seen in the data taken with the highest spectral resolution. It is clearly observed in the X-SHOOTER 2016 spectra and to lesser extent in the ISIS 2014 spectra, which has a poorer spectral resolution. To determine the radial velocities of the $H\alpha$ absorption-line, we

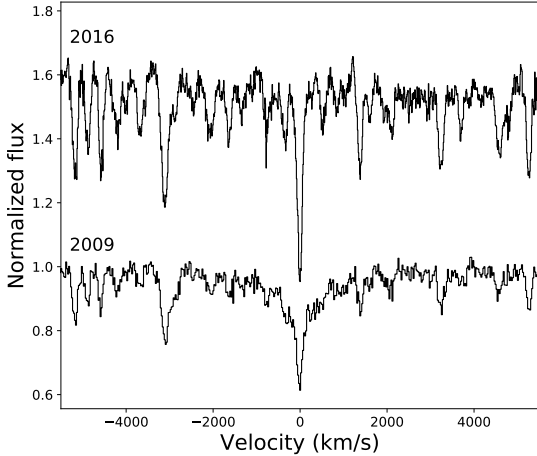
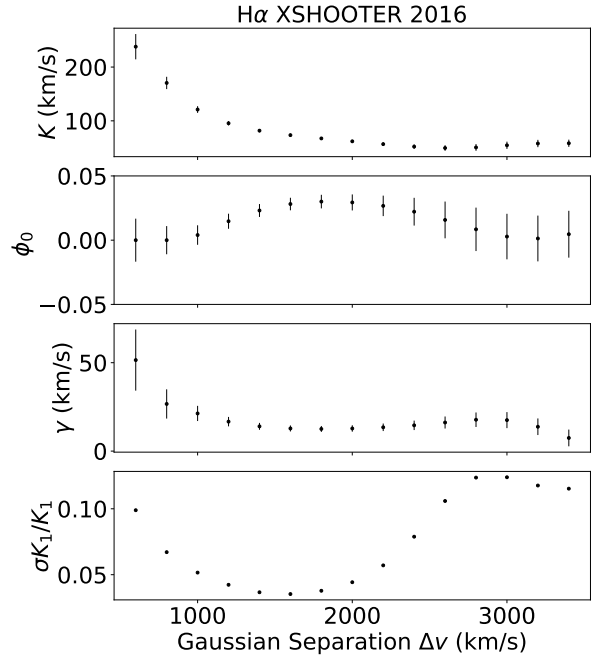


Figure 8. Isolating the narrow H α narrow absorption component arising from the secondary star in PSR J1023+0038. We show the average H α profile in the rest frame of the system’s centre-of-mass (top) and the average spectrum of the secondary star without the accretion disc profile, showing the narrow H α absorption component (bottom). The spectra have been offset for clarity.

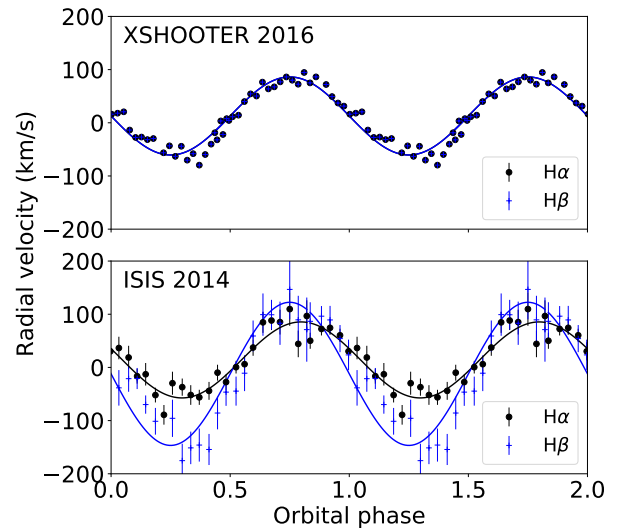
cross-correlate each individual target spectrum with a rotationally broadened H α absorption-line profile, using only the region around H α . We then perform a least-squares fit of the radial velocities versus orbital phase using an eccentric orbit and determine the radial velocity semi-amplitude $K_{2,H\alpha}$ (see Section 4). For the ISIS 2014 and X-SHOOTER 2016 disc-state spectra, before we perform the cross-correlation, we isolate the narrow H α absorption-line by subtracting the average accretion disc profile. The narrow H α absorption-line is not clearly resolved in the ISIS 2014 spectra, mainly due to the spectral resolution of the data, and so we only analyse the X-SHOOTER 2016 spectra. In Fig. 4 (right) we show the radial velocity curves obtained from the ISIS 2009 and X-SHOOTER 2016 spectra, where we measure $K_{2,H\alpha}=270.4\pm 5.4$ and 293.6 ± 4.2 km s $^{-1}$, respectively (the 1σ errors are quoted where the error bars have been rescaled so that the reduced χ^2 of the fit is 1). The ISIS 2009 radial velocity curve is consistent with a circular orbit, however, the X-SHOOTER 2016 radial velocity curve is eccentric. It is not clear if this eccentricity is real or if it is due to the uncertainty in disentangling the narrow H α absorption-line modulation from the double-peaked disc emission-line profile. In Fig. 8 the average Doppler-corrected H α absorption-line spectrum of the X-SHOOTER 2016 and ISIS 2014 spectra in the rest frame of the secondary star are shown.

6 DOPPLER MAPS

Doppler tomography is used to deduce the accretion structures in binary systems (see Marsh 2001, for a review). The method inverts phase-resolved spectra into an equivalent image of brightness distribution in velocity space (Marsh & Horne 1988). It is able to separate various sources of emission, such as from the secondary star or accretion disc, in velocity space. Some of the basic assumptions of Doppler tomography are that velocity vectors rotate with the binary, motion is parallel to the orbital plane and the flux from any point is constant in time. Violations of these assumptions do not imply that Doppler tomography cannot be performed, but care must be taken when interpreting the Doppler maps.



(a) Diagnostic diagram.



(b) Emission-line radial velocity curves.

Figure 9. (a) An example of the diagnostic diagram for the H α emission line of the X-SHOOTER 2016. The panels show the fitted sine-wave parameters as a function of the Gaussian separation $\Delta\nu$. (b) The optimal result of the double-Gaussian technique to measure the H α (black) and H β (blue) emission-line radial velocity curve. The resulting best-fit sinusoidal model is shown (solid line). We show the results for the X-SHOOTER 2016 (top) and ISIS 2014 (bottom) disc-state spectra.

To compute the Doppler maps of PSR J1023+0038 we used the normalised continuum subtracted spectra and the Python/C++ maximum entropy Doppler tomography code⁴ developed by T. Marsh. We model both absorption and emission-line modulated components. In Fig. 7 we show the trailed spectra and Doppler maps of the

⁴ <https://github.com/trmrsh/trm-doppler>

H α emission-line seen in the 2014 and 2016 disc-state. We also compute the Doppler map of the ISIS 2009 pulsar-state spectra, which shows the narrow H α absorption-line arising from the secondary star. We do not compute the Doppler maps of the H β and other lines because the ISIS 2009 and 2014 spectra do not have sufficient signal-to-noise for a comparison with the X-SHOOTER spectra. The disc-state trailed spectra show the characteristic double-peaked tramlines, a signature of a Keplerian accretion disc, that show up as a constant emission ring-like structure of high intensity in the Doppler maps. The trailed spectra also show a narrow absorption, which is in phase with the secondary star, and a narrow emission-line feature which is shifted by ~ 0.1 phase with respect to the secondary star, which arises from the accretion disc. Indeed, the crossing of this emission-line feature with the H α absorption-line feature at orbital phase ~ 0.7 seems to be responsible for the larger deviations observed in the H α velocities (see Fig. 4). The relative strength of the blue and red emission-line peaks vary over the orbital period, and results in an axisymmetric Doppler map with enhanced emission between orbital phase 0.25 and 0.50.

6.1 The neutron star's radial velocity

The emission lines generated from a uniform symmetric accretion disc around a neutron star will have the same velocity shift as the neutron star. The centroids of the lines will produce a sinusoidal phase-dependent modulation corresponding to the orbital motion of the neutron star. The addition of other sources of phase-dependent modulation, such as from a bright spot, results in a radial velocity curve that is offset in phase with respect to the true motion of the neutron star. Therefore, in order to exclude these contributions, one examines the wings of the emission-line profile corresponding to material orbiting at small disc radii from the neutron star, where the contamination by other sources are assumed to be minimal.

To measure the radial velocities of the Balmer emission lines we use the well established double-Gaussian technique of [Schneider & Young \(1980\)](#). This technique allows one to extract radial velocity curves from the wings of the emission-line profile, which are expected to follow the motion of the neutron star. By convolving the emission-line with double-Gaussian function with varying separation the radial velocity curve is determined. We apply this technique to the high spectral resolution ISIS 2014 and the X-SHOOTER 2016 spectra, where we can clearly see the double-peaked emission-line profile from the accretion disc. We use a Gaussian width of 600 km s^{-1} and vary the separation Δv from 600 to 3600 km s^{-1} in steps of 200 km s^{-1} . At each Gaussian separation the resulting radial velocity curve was fitted with a sine function of the form

$$V = \gamma - K \sin[2\pi(\phi - \phi_0)] \quad (2)$$

where V is the radial velocity, K the velocity semi-amplitude, γ the systemic velocity, ϕ the orbital phase, and ϕ_0 is the phase at superior conjunction of the neutron star. The results of the radial velocity analysis as well as the fractional error in the amplitude ($\sigma K/K$), which is a function of the Gaussian separation, are inspected in the form of a diagnostic diagram ([Shafter et al. 1986](#)). By plotting such a diagram it is possible to select the value of K that most closely represents the actual K_1 . The point beyond which the noise in the continuum begins to dominate the signal from the emission-line wings corresponds to a sharp increase in $\sigma K/K$. Usually K_1 obtained from a diagnostic diagram is the value corresponding to when $\sigma K/K$ is at a minimum (see Fig. 9a). For the H α emission-line we obtain $K_1 = 72 \pm 5 \text{ km s}^{-1}$ and $\phi_0 = 0.05 \pm 0.01$, whereas for the

H β emission-line we obtain $K_1 = 135 \pm 9 \text{ km s}^{-1}$ and $\phi_0 = 0.05 \pm 0.01$ for the ISIS 2014 spectra (see Fig. 9b). For the X-SHOOTER 2016 spectra we obtain $K_1 = 73 \pm 3 \text{ km s}^{-1}$ and $\phi_0 = 0.028 \pm 0.005$ using the H α emission-line and $K_1 = 118 \pm 6 \text{ km s}^{-1}$ and $\phi_0 = 0.050 \pm 0.007$ using the H β emission-line. Note that the H α and H β K_1 values for the 2014 and 2016 spectra are consistent with each other.

7 DISCUSSION

7.1 The neutron star's radial velocity

The projected semi-major axis of the pulsar orbit measured from radio timing observations, $x_1 = a_1 \sin i = 0.343356$ light-seconds ([Jaodand et al. 2016](#)) allows one to determine the radial velocity semi-amplitude of the neutron star $K_1 = 2\pi c x_1 / P_{\text{orb}} = 38 \text{ km s}^{-1}$ (where a is the binary separation and c is the speed of light). The fact that we obtain K_1 values (see Section 6.1) that are different for the H α and H β emission lines wings with relatively large phase offsets, which do not agree with the expected value derived from radio timing, means that the wings of the emission-line profiles do not follow the motion of the neutron star. Indeed, it has been shown that bright-spot non-Keplerian motion can induce a measured K_1 larger than the true value ([Smak 1970](#); [Paczynski et al. 1968](#)). The motion of the emission lines reflect the region where that emission lines are excited, further out in the accretion disc.

7.2 Doppler maps

The X-ray and optical flaring mode-switching behaviour of PSR J1023+0038 in the disc-state has been extensively studied by a number of authors ([Linares 2014](#); [Tendulkar et al. 2014](#); [Bogdanov 2015](#); [Shahbaz et al. 2015](#)). The optical and X-ray passive and active mode-switching behaviour have transition time-scales of $< 20 \text{ s}$, and it has been suggested that they are due to fast of a propeller, where matter in the disk in-flow is propelled away by the rapidly rotating neutron star magnetosphere ([Campana et al. 2016](#)).

[Hakala & Kajava \(2018\)](#) were able to isolate the passive and active-state spectra from time resolved H α spectroscopy taken in 2017. Narrow H α absorption-line feature can be clearly seen in the active-state spectra, which is not present in the passive-state spectra. They also found evidence for a lack of H α emission around orbital phase 0.25–0.50 in the active-state and interpret it as matter being ejected from the system via the propeller effect ([Wynn et al. 1997](#)). Our 2014 and 2016 observations also shows narrow H α absorption-line feature but in contrast to [Hakala & Kajava \(2018\)](#) we observe excess H α emission around orbital phase 0.25–0.50. Note that [Hakala & Kajava \(2018\)](#) use the orbital ephemeris given in [Jaodand et al. \(2016\)](#), which agrees with our ephemeris (see Table 2).

7.3 Accretion disc size

One can estimate the inner and outer accretion disc radii in accreting MSPs by measuring the emission-line wing and peak separations, respectively. The Keplerian velocity of an annulus of gas in Keplerian motion at radius r around a neutron star of mass M_1 orbiting at an inclination angle i is given by

$$V_{\text{kep}} = \sqrt{\frac{GM_1}{r}} \sin i. \quad (3)$$

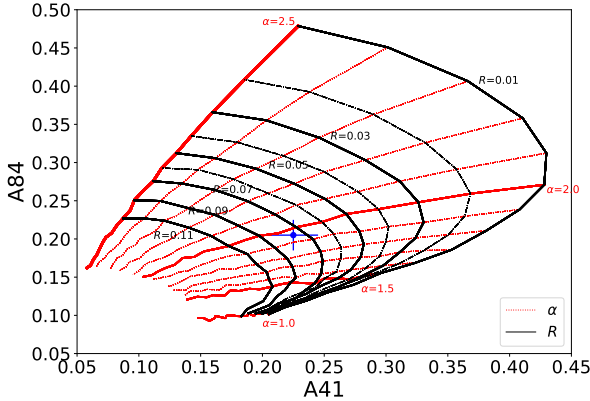


Figure 10. Theoretical [A84,A41] values measured from the accretion disc $H\alpha$ emission-line profile for each $[\alpha, R]$ pair (Smak 1981). The red and black lines represent constant α and R , respectively. Our observed $H\alpha$ value is shown as the solid filled blue circle.

For a double-peaked emission-line profile from an accretion disc, the Keplerian velocity of the outer disc radius (r_{out}) corresponds to half the peak-to-peak separation, while the Keplerian velocity at the inner accretion disc radius (r_{in}) corresponds to half the wing separation (full width at zero intensity). We measure velocities using spectra in which the wings and peaks of the accretion disc emission-line are not affected by bright-spot emission or absorption from the secondary star, which is around orbital phase 0.0. We use the average 2016 X-SHOOTER disc-spectra taken around orbital phase 0.0 and measure the $H\alpha$ half peak-to-peak separation and half wing separation to be $367 \pm 6 \text{ km s}^{-1}$ and $\sim 2000 \text{ km s}^{-1}$, respectively. Note that the wing separation is difficult to establish because of the uncertainty in where the line wings end and the continuum begins and possible contamination from other absorption and disc emission lines. We estimate the ratio $R = r_{\text{in}}/r_{\text{out}}$ to be ~ 0.03 . However, it should be noted that there is clear evidence from studies of cataclysmic variable that the for the outer disc is sub-Keplerian (Wade & Horne 1988) and so R is underestimated. Accounting for this ~ 20 per cent effect, gives $R \sim 0.04$.

We can also estimate R using the method developed by Smak (1981). Smak’s method assumes an axially symmetric accretion disc in Keplerian motion and a power-law flux distribution $f \propto r^{-\alpha}$ for the disc emission. He found a relationship between the pairs [A84,A41] and $[\alpha, R]$, where parameters $A84 = \log W_{0.4} - \log W_{0.8}$ and $A41 = \log W_{0.1} - \log W_{0.4}$ can be measured from the emission-line profile ($W_{0.8}$, $W_{0.4}$ and $W_{0.1}$ are the emission-line widths at the fractions 0.8, 0.4 and 0.1 of the peak height above the continuum, respectively). We apply Smak’s method to the average 2016 X-SHOOTER $H\alpha$ disc-state spectrum taken around orbital phase 0.0. In Fig. 10 we show the theoretical [A84,A41] pairs for a given $[\alpha, R]$ as well as our observed values, [A84,A41] = [0.19,0.22], which corresponds to $R \sim 0.075$ and $\alpha \sim 2.0$.

Assuming that the accretion disc radius does not exceed the maximum disc radius determined by tidal interactions with the secondary star, approximated by $r_{\text{tidal}}/a = 0.6/(1+q) \sim 0.94 R_{\odot}$ ($q=0.141$, $M_1+M_2=2.0 M_{\odot}$ and a is the binary separation; Warner 2003), and $R \sim 0.040-0.075$, we estimate $r_{\text{in}} \sim 0.04-0.07 R_{\odot} \sim 26,000-50,000 \text{ km}$. This is the location of the inner disc radius that produces the bulk of the $H\alpha$ emission which lies further out from

from the inner edge of the accretion disc $\sim 150 \text{ km}$ (Archibald et al. 2009; Deller et al. 2012).

Wang et al. (2009) also estimate r_{in} by modelling the 2001 disc-state continuum spectrum with a simple accretion disc model. They obtained $r_{\text{in}} \sim 14,000 \text{ km}$, which is about a factor of 2 closer to the neutron star compared to what we measure from our 2016 disc-state spectrum. However, it should be noted that the 2001 spectrum (Wang et al. 2009) was taken just before PSR J1023+0038 switched to the pulsar-state sometime between 2001–2003 (Woudt et al. 2004), whereas our 2016 spectrum was just after PSR J1023+0038 transitioned into the disc-state in 2013 (Stappers et al. 2014). This suggests that during the extended period of accretion in the disc-state, the region responsible for the $H\alpha$ emission drifts inwards towards the neutron star, before transitioning to the pulsar-state.

7.4 A peculiar secondary star

In Fig. 11 we show the variance-weighted Doppler-averaged spectrum of PSR J1023+0038 taken in 2009 and 2016, as well a G5V template star artificially broadened by 75 km s^{-1} for comparison. As one can see, the pulsar-state 2009 spectrum shows deeper absorption lines compared to the F8 or G5V star, in particular the Ca I lines at 6439.075 \AA , 6493.781 \AA and Ca I 6462.567 \AA , and the $\sim 6495 \text{ \AA}$ blend of Ca I 6493.781 \AA , Fe I 6494.980 \AA and Ba II 6496.897 \AA . This can also be seen in the value for f_{star} obtained in Section 4, which are all greater than 1 for all spectral type. A full chemical analysis is beyond the scope of this paper, but we compare the observed PSR J1023+0038 spectrum with synthetic high-resolution spectra from the PHOENIX library (Husser et al. 2013). We show the synthetic spectrum for a 5600 K $\log g=4.5$ star with a metallicity Z of -1.0 , 0.0 and $+1.0$. We find that the 2016 disc-state spectrum of PSR J1023+0038 and the G5V spectrum are reasonably well described by the $Z=0.0$ synthetic spectrum. However, the 2009 pulsar-state spectrum is better described by the $Z=+1.0$ synthetic spectrum. Fe and Ca seems to be over-abundant in the atmosphere of the secondary star, and so makes the secondary star in PSR J1023+0038 peculiar. In general the features in the 2009 pulsar-state spectrum are ~ 5 times stronger than in the 2016 disc-state spectrum.

7.5 Spectral type changes along the orbit

The light curves taken when PSR J1023+0038 was in the pulsar-state (Woudt et al. 2004; Thorstensen & Armstrong 2005) show an asymmetric single-humped modulation, which is expected from the combined effects of the tidally-locked secondary star’s ellipsoidal modulation and the high-energy emission from the pulsar wind heating of the inner face of the secondary star. The light curve observed in the disc-state is very similar in shape and amplitude (Kennedy et al. 2018), suggesting that the effect of heating on the secondary star is the same when the system is in the pulsar- or disc-state and that the main source of irradiation of the secondary star is the high-energy emission from the pulsar relativistic wind. The asymmetric maximum suggests that the heating does not come directly from the isotropic pulsar wind, but is due to non-thermal X-ray emission produced by the intra-binary shock between the pulsar and secondary star’s wind (Romani & Sanchez 2016).

Given that heating with a bolometric irradiating luminosity of $10^{34} \text{ erg s}^{-1}$ (McConnell et al. 2015) has a pronounced effect on the phase-resolved V-band light curves in the pulsar-state, we expect to see similar effects on the phase-resolved spectroscopy. Indeed, the 2016 disc-state spectra show evidence for a spectral

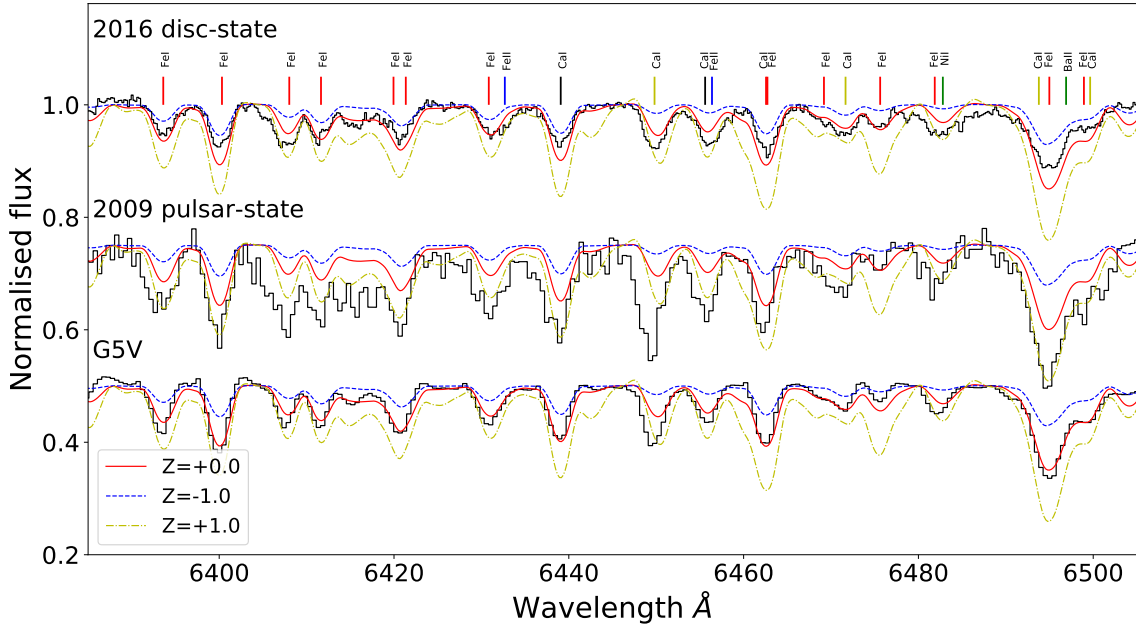


Figure 11. A comparison of the PSR J1023+0038 pulsar- and disc-state spectrum with synthetic spectra. From top to bottom: the 2016 disc-state, 2009 pulsar-state spectrum and the spectrum of a rotationally-broadened G5V star. We also over-plot the rotationally broadened synthetic spectra of a 5600 K $\log g=4.5$ star with $Z = -1.0$ (blue dashed line), $+0.0$ (red solid line) and $+1.0$ (yellow dot-dashed line). The observed spectra have been shifted to the rest frame of the synthetic spectrum.

type change across the orbit, from G5 at phase 0.0 to F6 at phase 0.5, corresponding to a temperature change of 5650 K to 6340 K, respectively (Pecaut & Mamajek 2013). This is also supported by the significant eccentric fit to the metallic absorption-line radial velocity curve (see Table 2), where irradiation distorts the radial velocity curve of the secondary star, as the centre-of-light of the absorption lines changes with orbital phase. Significant eccentric orbits are not detected in the 2009 pulsar-state and 2014 disc-state spectra, because of the lower quality and spectral resolution of the 2009 and 2014 spectra compared to the 2016 disc-state spectra. The moderate inclination angle of 54° of the system (McConnell et al. 2015) implies that the contrast between the observed spectral type at different orbital phases is reduced, which means that the observer always sees the heated inner face of the secondary star and thus the true spectral type of the secondary star is cooler. Simultaneous modelling of the optical light- and radial-velocity curves during the pulsar-state should reveal the true spectral type of the secondary star (Shahbaz et al. 2017; Linares et al. 2018)

7.6 The secondary star’s radial velocity curve

The absorption lines arising from the secondary star are Doppler shifted as the star moves in its orbit. Therefore, the radial velocity at a given orbital phase depends on the observed centre-of-light of the lines that are used to determine the radial velocities. Heating shifts the centre-of-light of the secondary, weighted by the strength of the absorption lines, from the centre-of-mass of the star. This results in a distortion of the radial velocity curve leading to an apparent elliptical/eccentric orbit with a spurious radial velocity semi-amplitude (Davey & Smith 1992; Shahbaz et al. 2000). Variable amounts of heating will produce different radial velocity semi-amplitudes.

In Fig. 12 we show the different values for $K_{2,Z}$ and $K_{2,H\alpha}$

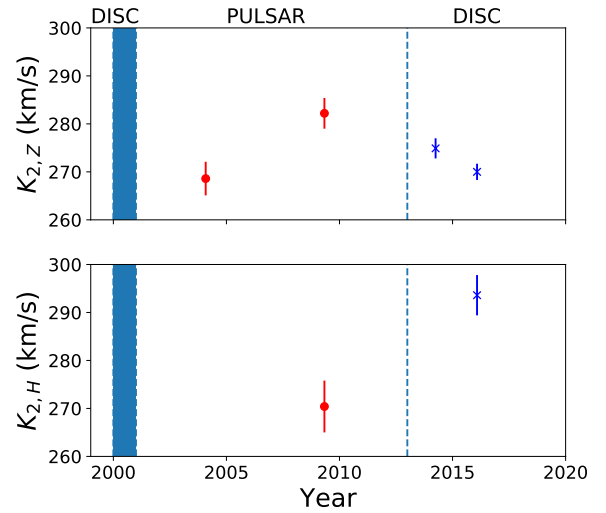


Figure 12. The observed secondary star’s metallic (top) and $H\alpha$ (bottom) absorption-line radial velocity semi-amplitude using optical spectra taken in 2004 and 2009 in the pulsar-state (filled red circles) and in 2014 and 2016 in the disc-state (blue crosses), respectively (see Table 2). The vertical band marks the time when the system transitioned from a MSP around 2000-2001 (Wang et al. 2009) and from a MSP to a LMXB in 2013 (Stappers et al. 2014).

determined between 2004 and 2016, when the system was either in the pulsar- (P) or disc- (D) state. The value for $K_{2,Z}^P$ determined in 2004 and 2009 in the pulsar-state are different at the 2.8σ level, and so we can assume that there is no significant change in $K_{2,Z}$

The value for $K_{2,Z}^D$ determined from the 2014 and 2016 spectra, when the system was in the disc-state are similar at the 1.8σ level, which is not surprising given that the X-ray and γ -ray flux are also very similar (see Fig. 1). During the 2009 to 2014 transition the change in $K_{2,Z}$ is only significant at the 1.9σ level. However, the 2009 to 2016 transition the change in $K_{2,Z}$ is significant at the 3.4σ level which can be explained by the accretion disc shadowing (see Section 7.6.2).

7.6.1 The pulsar-state radial velocity curve

We can use our X-ray binary model `XRBCURVE` (Shahbaz et al. 2003, 2017) to determine the line flux distribution and hence radial velocity curve arising from the secondary star in PSR J1023+0038, for a system in the pulsar- and disc-state, where one may expect different amounts of heating. An important parameter that determines the shape and amplitude of the radial velocity curve is the effects of heating and how the line-strength versus temperature relation used in determining the radial velocity. We assume the "deep heating" approximation which means that each element radiates as predicted by a model atmosphere for a single star. The spectral type of the secondary stars in MSPs and X-ray binaries are typically later than F and their spectra contain metal absorption lines. The strongest absorption metallic lines in the red part of the optical spectrum are the Fe I, Ca I and Ba II lines (see Fig. 11). Using UVESPOP spectra we find that the line strength versus temperature relation of the metallic absorption lines in the 6000–6500 Å spectral range decreases with increasing temperature. Similarly, for the H α absorption-line (Balmer), we find that the line strength increases with increasing temperature (Shahbaz et al. 2017; Linares et al. 2018). Therefore, we can compute the secondary star's metallic ($K_{2,Z}$) or Balmer ($K_{2,H}$) absorption-line radial velocity semi-amplitude. Equations 4a to 4e are the conditions we find due the effects of irradiation and/or accretion disc on the metallic and Balmer line radial velocity curves semi-amplitudes.

$$K_{2,Z}^P > K_{2,H}^P \quad (4a)$$

$$K_{2,Z}^D > K_{2,H}^D \quad (4b)$$

$$K_{2,Z}^D < K_{2,Z}^P \quad (4c)$$

$$K_{2,H}^D > K_{2,H}^P \quad (4d)$$

$$K_{2,Z}^D > K_{2,H}^D \quad (4e)$$

In the pulsar-state, high energy relativistic particles produced by the pulsar wind are mostly likely responsible for heating the secondary star's inner face. The hot inner face thus produces less metallic line flux compared to the non-heated face of the star, and so the centre-of-light is shifted towards the non-heated side of the star, resulting in a spuriously high radial velocity semi-amplitude; $K_{2,Z}^P > K_{2,H}^P$. In Fig. 13a we show the metallic and Balmer absorption-line radial velocity curve deviations. The model predicts that the metallic radial velocity semi-amplitude is greater than the Balmer radial velocity semi-amplitude in both the pulsar- and disc-states (see Equation 4a). In contrast, the hot inner face produces more Balmer flux on the heated face compared to the non-heated face of the star, and so the centre-of-light is shifted towards the heated side of the star, resulting in a spuriously low radial velocity semi-amplitude; $K_{2,H}^P < K_{2,Z}^P$. Our ISIS 2009 observations in the pulsar-state imply $270.4 < K_2 < 282.2 \text{ km s}^{-1}$ (or $K_2 = 276.3 \pm 5.6 \text{ km s}^{-1}$).

7.6.2 The pulsar- to disc-state radial velocity

The pulsar- to disc-state transition involves an increase in the gamma-ray and X-ray flux (Takata et al. 2014), resulting in a change in the metallic and Balmer line radial velocity semi-amplitude because of the effects of the accretion disc shadowing. In Fig. 13b we show the effects the accretion disc has on the shape of the metallic absorption-line profile. We show the simulated line profile in the pulsar- and disc-state observed at orbital phase 0.25. The elements of area near the inner Lagrangian point contribute flux to the negative wing of the line profile. We assume a bolometric irradiating luminosity of $10^{34} \text{ erg s}^{-1}$ which is the same in the pulsar- and disc-state. In the pulsar-state elements of area on the hot irradiated inner face of the star produce less metallic line flux (because of the line-strength versus temperature relation) compared to the non-heated face of the star, and so the centre-of-light of the line profile (blue solid line) is shifted towards the non-heated side of the star. The appearance of an accretion disc shadows the elements area near the inner Lagrangian point (negative wing of the line profile at phase 0.25), which intrinsically have lower temperatures because of gravity darkening, and so contribute more flux than in the pulsar-state. The line profile is skewed and the effect of the disc shadowing is to shift the centre-of-light of the line profile towards the inner Lagrangian point, resulting in a lower radial velocity semi-amplitude compared to in the pulsar-state (see Equation 4c). For the H α absorption-line, the opposite line-strength versus temperature relation implies that the centre-of-light of the absorption-line profile is shifted away from the inner Lagrangian point. This results in a higher semi-amplitude compared to when there is no accretion disc (see Equation 4d). Finally the accretion disc shadowing also gives the condition in Equation 4e.

We find that the 2009 pulsar-state data satisfies equation 4a and the metallic and Balmer radial velocities determined from the 2009 to 2014/2016 transition satisfies equation 4c and 4d, respectively. However, the 2016 disc-state data does not satisfy equation 4b or 4e, but this could be due to problems in disentangling the narrow H α absorption-line modulation from the double-peaked disc emission-line profile. Therefore the observed changes in the $K_{2,Z}$ and $K_{2,H}$ in the pulsar- and disc-state can be explained to some extent by the presence of an accretion disc.

7.7 The Roche lobe filling factor in the pulsar-state

In contrast to the disc-state, in the pulsar-state no accretion disc is present and hence the secondary star does not fully fill its Roche lobe. Indeed, observations of the MSP secondary stars in the pulsar-state show that they underfill their Roche lobes; the Roche lobe filling factor is in the range $f_{\text{Roche}}=0.80\text{--}0.95$ (Shahbaz et al. 2017; Linares et al. 2018). Given that the star's rotational broadening depends on its radius, the star's radius is smaller in the pulsar-state compared to in the disc-state. It can be shown that the star's equivalent volume radius depends on the binary mass ratio and Roche lobe filling factor, as well as its radial velocity semi-amplitude (Shahbaz et al. 2017). Using equation (2) in Shahbaz et al. (2017) we can calculate the change in the rotational broadening for different values of f_{Roche} ($q=0.14$, see Section 7.6.2) and compare it to the observed change in $v_{\text{rot}} \sin i$. Given the observed X-ray/gamma-ray luminosities, the effects of irradiation in the determination of $v_{\text{rot}} \sin i$ in the two states are similar and so appropriately cancel out. In Section 5 we determine the secondary star's rotational broadening in the pulsar-state to be larger than in the disc-state (see Table 2). However, it should be noted that the pulsar-state $v_{\text{rot}} \sin i$ measure-

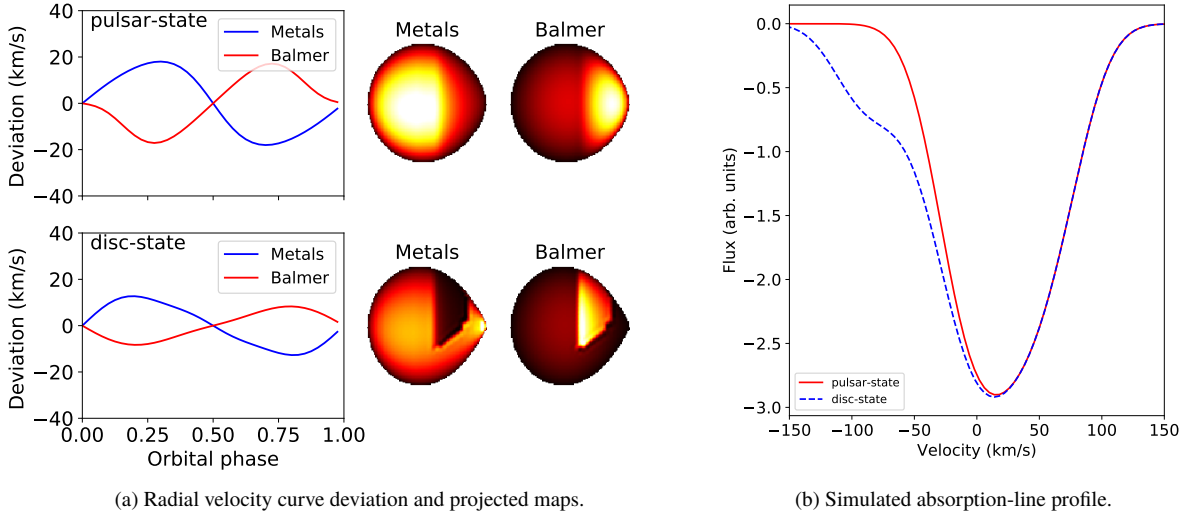


Figure 13. (a) We show the apparent radial velocity curve deviation from a circular orbit for the pulsar-state (top panel) and disc-state (bottom panel). In each panel we plot the radial velocity deviation using the metallic absorption lines in the 6000–6500Å spectral range (solid blue) and the Balmer absorption line (dashed red). We assume a $T_{\text{eff}}=5660$ K secondary star, $q=0.14$, $i=43^\circ$, $K_2=270$ km s $^{-1}$ and $L_X = 10^{34}$ erg s $^{-1}$. For the pulsar-state we assume $f_{\text{Roche}}=0.83$, with no accretion disc and for the disc-state we assume $f_{\text{Roche}}=1$ and an accretion disc that extends to the tidal radius with an opening angle of 20° . On the right we show projected maps of the observed metallic and Balmer line-strength distribution on the secondary star at orbital phase 0.75 using `xrbcurve` (Shahbaz et al. 2003, 2017). (b) We show the simulated absorption-line profile in the pulsar-state (red solid line) and disc-state (blue dashed line), observed at orbital phase 0.25. The same model parameters as above are used. Note the change in the line profile shape.

ment has a large error. The ratio of pulsar-state to disc-state $v_{\text{rot}} \sin i$ value is 1.037 ± 0.038 . Using the 3σ lower limits, we find a change in $v_{\text{rot}} \sin i$ of >0.923 , which corresponds to a Roche lobe filling factor of $f_{\text{Roche}} > 0.78$, agreeing with what was obtained by McConnell et al. (2015) by modelling the V-band light curve obtained by Thorstensen & Armstrong (2005) in the pulsar-state.

7.8 Irradiating luminosity

In the pulsar- and or disc-state, the relativistic pulsar wind and and/or X-ray/gamma-ray emission from the accretion disc are the dominant sources of irradiation. We can compute the irradiating luminosity temperature difference of hemispheres of the secondary star and compare it to the observed X-ray and gamma-ray luminosities, as well as to the pulsar’s spin down luminosity (L_{sd}) and determine the source of the driving mechanism. The “irradiation temperature” is given by $T_{\text{irr}}^4 = T_{\text{day}}^4 - T_{\text{night}}^4$, where T_{night} and T_{day} are the temperatures observed at orbital phase 0.0 and 0.5, respectively. The irradiating luminosity is then $L_{\text{irr}} = 4\pi a^2 \sigma T_{\text{irr}}^4$ where a is the orbital separation, which is related to L_{sd} via the efficiency of irradiation parameter; $\eta_{\text{irr}} = L_{\text{irr}}/L_{\text{sd}}$. Using $T_{\text{night}}=5650$ K and $T_{\text{day}}=6340$ K (Pecaut & Mamajek 2013) we find $T_{\text{irr}}=4943$ K and $L_{\text{irr}} = 6.5 \times 10^{33}$ erg s $^{-1}$, which implies $\eta_{\text{irr}}=14$ percent. For PSR J1023+0038 in the disc-state, the observed X-ray (0.5–10 keV) luminosity is 2×10^{33} erg s $^{-1}$ (Takata et al. 2014), the gamma-ray (0.2–20 GeV) luminosity is 6×10^{33} erg s $^{-1}$ (Stappers et al. 2014) and the pulsar’s spin-down luminosity (corrected for the Shklovskii effect) is $L_{\text{sd}} = 4.8 \times 10^{34}$ erg s $^{-1}$ (Strader et al. 2018). The irradiation efficiency of 14 percent we derive is similar to what is observed in other MSPs Breton et al. (2013). Indeed, the energetics suggest that the pulsar’s the relativistic wind, powered by the rotational spin down of the neutron star can drive the observed heating mechanism in the disc-state. However, in PSR J1023+0038 the observed X-ray and gamma-ray (most

likely due to accretion) luminosities are also sufficient to provide the observed irradiating luminosity.

7.9 The system parameters

Archibald et al. (2009) determined the binary mass ratio of $q=0.141 \pm 0.002$ ($q=K_1/K_2$) by measuring the radial velocity semi-amplitude of the neutron star determined from radio timing $K_1=38$ km s $^{-1}$ and the secondary star’s radial velocity semi-amplitude 268 ± 4 km s $^{-1}$ determined by (Thorstensen & Armstrong 2005). We update this value using our K_2 value determined in Section 7.6.1 to obtain $q=0.137 \pm 0.003$. We can also determine the mass ratio from the fact that the Roche lobe filling star’s rotational broadening radius depends only q and K_2 in the disc-state (Wade & Horne 1988; Shahbaz et al. 2017). Using $v_{\text{rot}} \sin i = 74.9 \pm 0.9$ km s $^{-1}$ and our K_2 value we obtain $q=0.20 \pm 0.03$. It should be noted that this value is uncertain because the limb-darkening coefficient used in the determination of $v_{\text{rot}} \sin i$ leads to an overestimation of secondary star’s rotational broadening. Also, irradiation leads to an underestimation of $v_{\text{rot}} \sin i$ (see Shahbaz 2003, and references within). Despite this, the value for q is consistent, at the $2\text{-}\sigma$ level, with the revised value determined earlier.

From the mass function equation, one can use K_2 , q , the orbital period and the binary inclination i to determine the masses of the compact object and secondary star (M_2). Using our values for $K_2 = 276.3 \pm 5.6$ km s $^{-1}$ and $q=0.137 \pm 0.003$ we obtain

$$M_1 = \frac{0.56 \pm 0.03}{\sin^3 i} M_\odot, \quad M_2 = \frac{0.077 \pm 0.005}{\sin^3 i} M_\odot \quad (5)$$

For a neutron star with a mass in the range 1.4 to 3 M_\odot , corresponding to the canonical and maximum theoretical mass of a neutron star (Chamel et al. 2013), respectively, implies i between 47 and 35° , respectively.

Thorstensen & Armstrong (2005) modelled the multi-colour (B , V and I) optical lightcurves of PSR J1023+0038 in the 2009 pulsar-state with a fully Roche-lobe filling irradiated secondary star model. They noted that assuming that if the secondary fills its Roche lobe its mass can be inferred from the distance (D_{kpc}), because the distance determines the temperature and size of the star. If the star underfills its Roche lobe then $D_{\text{kpc}} < 2.20(M_2/M_\odot)^{1/3}$. Deller et al. (2012) used this relation with K_2 measured by Thorstensen & Armstrong (2005), K_1 from radio timing and the distance D_{kpc} of 1.37 kpc from the known radio parallax to determine M_1 . We use the same method but with our revised values for K_2 and q to obtain $M_1 > 1.76 \pm 0.16 M_\odot$, $M_2 > 0.24 \pm 0.02 M_\odot$ and $i < 43 \pm 2^\circ$. The mass estimates are lower limits because the secondary star in the pulsar-state can substantially underfill its Roche lobe.

The V -band optical lightcurve and a radial velocity curve presented in Thorstensen & Armstrong (2005) was also modelled by McConnell et al. (2015). Allowing for the secondary star's Roche lobe filling factor to vary, they find that the secondary star underfills its Roche lobe and $i \sim 54 \pm 5^\circ$. This inclination angle is much higher than what we estimate above and gives an unusually low mass for the neutron star; $M_1 = 1.1 \pm 0.2 M_\odot$. Given that we expect relatively massive ($\sim 1.8 M_\odot$) neutron stars to reside in MSPs, (Strader et al. 2018) we suspect their determination of i is biased. Simultaneous modelling of multi-band lightcurves with high resolution spectroscopy is needed. This will allow one to determine effective temperature of the secondary, its true radial velocity semi-amplitude, inclination angle and hence the mass of the neutron star.

CONCLUSIONS

We present time-resolved optical spectroscopy of the binary millisecond pulsar PSR J1023+0038 during its 2009 radio-powered pulsar-state and during its accretion-powered disc-states in 2014 and 2016. Below we list the main results of this paper.

(i) We provide observational support for the companion star being heated during the disc-state. We observe a spectral type change along the orbit, from $\sim G5$ to $\sim F6$ at the secondary star's superior and inferior conjunction, respectively, which correspond to the "day" and "night" side temperatures of the secondary star. We find that the irradiating luminosity can be powered by the spin down luminosity of the neutron star, as is the case on many other MSPs, or by the accretion luminosity of the accretion disc.

(ii) We determine the secondary star's radial velocity semi-amplitude from the metallic (primarily Fe and Ca) and $H\alpha$ absorption lines during the pulsar- and different disc-states. We find that the observed changes in the metallic radial velocity semi-amplitude is only significant (at the 3.4σ level) for the 2009 pulsar-state to 2016 disc-state transition, which can be explained by the accretion disc shadowing. The metallic and $H\alpha$ radial velocity semi-amplitude determined from the 2009 pulsar-state observations allows us to constrain the secondary star's true radial velocity $K_2 = 276.3 \pm 5.6 \text{ km s}^{-1}$ and the binary mass ratio $q = 0.137 \pm 0.003$.

(iii) Doppler maps of the disc-state spectra show characteristic double-peaked emission-line profile arising from the accretion disc, a narrow absorption, which is in phase with the secondary star, and a narrow emission-line feature which is shifted by ~ 0.1 phase with respect to the secondary star, which arises from the accretion disc. From the average emission-line profile of the accretion disc in 2016, we place constraints on the inner to outer disc radii ratio, $0.04\text{--}0.075$.

(iv) By comparing the observed metallic and $H\alpha$ absorption-line radial velocity semi-amplitudes with model predictions, we can

explain the observed semi-amplitude changes during the different pulsar states and during the pulsar/disc-state transition as being due to different amounts of heating and the presence of an accretion disc, respectively.

ACKNOWLEDGEMENTS

We thank Tom Marsh for the use of his MOLLY, PAMELA and Doppler tomography programs. We acknowledge the use of data from the UVES Paranal Observatory Project (ESO DDT Program ID 266.D-5655). M.L. is supported by EU's Horizon 2020 programme through a Marie Skłodowska-Curie Fellowship (grant No. 702638). Based on observations made with the WHT telescope operated by the Instituto de Astrofísica de Canarias in the Spanish Observatories of el Roque de los Muchachos (La Palma). Based on observations made with ESO Telescopes at the La Silla Paranal Observatory under ESO programme 096.D-0808. This paper makes use of data obtained from the Isaac Newton Group Archive which is maintained as part of the CASU Astronomical Data Centre at the Institute of Astronomy, Cambridge. The Starlink software (Currie et al. 2014) is currently supported by the East Asian Observatory.

Facilities: WHT (ISIS), WHT (ACAM), VLT (X-SHOOTER)

References

- Al-Naimiy H. M., 1978, *Ap&SS*, **53**, 181
- Alpar M. A., Cheng A. F., Ruderman M. A., Shaham J., 1982, *Nature*, **300**, 728
- Archibald A. M., et al., 2009, *Science*, **324**, 1411
- Archibald A. M., Kaspi V. M., Hessels J. W. T., Stappers B., Janssen G., Lyne A., 2013, preprint, ([arXiv:1311.5161](https://arxiv.org/abs/1311.5161))
- Bagnulo S., Jehin E., Ledoux C., Cabanac R., Melo C., Gilmozzi R., ESO Paranal Science Operations Team 2003, *The Messenger*, **114**, 10
- Bassa C. G., et al., 2014, *MNRAS*, **441**, 1825
- Bogdanov S. e. a., 2015, *ApJ*, **806**, 148
- Bogdanov S., Archibald A. M., Hessels J. W. T., Kaspi V. M., Lorimer D., McLaughlin M. A., Ransom S. M., Stairs I. H., 2011, *ApJ*, **742**, 97
- Bond H. E., White R. L., Becker R. H., O'Brien M. S., 2002, *PASP*, **114**, 1359
- Breton R. P., et al., 2013, *ApJ*, **769**, 108
- Campana S., Coti Zelati F., Papitto A., Rea N., Torres D. F., Baglio M. C., D'Avanzo P., 2016, *A&A*, **594**, A31
- Chamel N., Haensel P., Zdunik J. L., Fantina A. F., 2013, *International Journal of Modern Physics E*, **22**, 1330018
- Currie M. J., Berry D. S., Jenness T., Gibb A. G., Bell G. S., Draper P. W., 2014, in Manset N., Forshay P., eds, *Astronomical Society of the Pacific Conference Series Vol. 485, Astronomical Data Analysis Software and Systems XXIII*. p. 391
- Davey S., Smith R. C., 1992, *MNRAS*, **257**, 476
- Deller A. T., et al., 2012, *ApJ*, **756**, L25
- Freudling W., Romaniello M., Bramich D. M., Ballester P., Forchi V., García-Dabó C. E., Moehler S., Neeser M. J., 2013, *A&A*, **559**, A96
- Fruchter A. S., Stinebring D. R., Taylor J. H., 1988, *Nature*, **333**, 237
- Gray D. F., 1992, *The observation and analysis of stellar photospheres.* Cambridge University Press
- Hakala P., Kajava J. J. E., 2018, *MNRAS*, **474**, 3297
- Halpern J. P., Gaidos E., Sheffield A., Price-Whelan A. M., Bogdanov S., 2013, *The Astronomer's Telegram*, **5514**
- Homer L., Szkody P., Chen B., Henden A., Schmidt G., Anderson S. F., Silvestri N. M., Brinkmann J., 2006, *AJ*, **131**, 562
- Horne K., 1986, *PASP*, **98**, 609
- Husser T.-O., Wende-von Berg S., Dreizler S., Homeier D., Reiners A., Barman T., Hauschildt P. H., 2013, *A&A*, **553**, A6

- Iglesias-Marzoa R., López-Morales M., Jesús Arévalo Morales M., 2015, *PASP*, **127**, 567
- Jaodand A., Archibald A. M., Hessels J. W. T., Bogdanov S., D'Angelo C. R., Patruno A., Bassa C., Deller A. T., 2016, *ApJ*, **830**, 122
- Kennedy M. R., Clark C. J., Voisin G., Breton R. P., 2018, *MNRAS*,
- Linares M., 2014, *ApJ*, **795**, 72
- Linares M., Casares J., Rodriguez-Gil P., Shahbaz T., 2014, The Astronomer's Telegram, 5868
- Linares M., Shahbaz T., Casares J., 2018, *ApJ*, **859**, 54
- Marsh T. R., 1989, *PASP*, **101**, 1032
- Marsh T. R., 2001, in Boffin H. M. J., Steeghs D., Cuypers J., eds, *Lecture Notes in Physics*, Berlin Springer Verlag Vol. 573, *Astrotomography, Indirect Imaging Methods in Observational Astronomy*. p. 1 ([arXiv:astro-ph/0011020](https://arxiv.org/abs/astro-ph/0011020))
- Marsh T. R., Horne K., 1988, *MNRAS*, **235**, 269
- Marsh T. R., Robinson E. L., Wood J. H., 1994, *MNRAS*, **266**, 137
- McConnell O., Callanan P., Kennedy M., Hurley D., 2014, in *The X-ray Universe 2014*. p. 133
- McConnell O., Callanan P. J., Kennedy M., Hurley D., Garnavich P., Menzies J., 2015, *MNRAS*, **451**, 3468
- Paczyński B., Piotrowski S. L., Turski W., 1968, *Ap&SS*, **2**, 254
- Papitto A., et al., 2013, *Nature*, **501**, 517
- Patruno A., et al., 2014, *ApJ*, **781**, L3
- Pecaut M. J., Mamajek E. E., 2013, *ApJS*, **208**, 9
- Radhakrishnan V., Srinivasan G., 1982, *Current Science*, **51**, 1096
- Romani R. W., Sanchez N., 2016, *ApJ*, **828**, 7
- Schneider D. P., Young P., 1980, *ApJ*, **238**, 946
- Shafter A. W., Szkody P., Thorstensen J. R., 1986, *ApJ*, **308**, 765
- Shahbaz T., 2003, *MNRAS*, **339**, 1031
- Shahbaz T., Groot P., Phillips S. N., Casares J., Charles P. A., van Paradijs J., 2000, *MNRAS*, **314**, 747
- Shahbaz T., Zurita C., Casares J., Dubus G., Charles P. A., Wagner R. M., Ryan E., 2003, *ApJ*, **585**, 443
- Shahbaz T., et al., 2015, *MNRAS*, **453**, 3461
- Shahbaz T., Linares M., Breton R. P., 2017, *MNRAS*, **472**, 4287
- Smak J., 1970, *Acta Astron.*, **20**, 311
- Smak J., 1981, *Acta Astron.*, **31**, 395
- Stappers B. W., et al., 2014, *ApJ*, **790**, 39
- Strader J., et al., 2018, arXiv e-prints,
- Szkody P. e. a., 2003, *AJ*, **126**, 1499
- Takata J., et al., 2014, *ApJ*, **785**, 131
- Tendulkar S. P., et al., 2014, *ApJ*, **791**, 77
- Thorstensen J. R., Armstrong E., 2005, *AJ*, **130**, 759
- Vernet J., et al. 2011, *A&A*, **536**, A105
- Wade R. A., Horne K., 1988, *ApJ*, **324**, 411
- Wang Z., Archibald A. M., Thorstensen J. R., Kaspi V. M., Lorimer D. R., Stairs I., Ransom S. M., 2009, *ApJ*, **703**, 2017
- Warner B., 2003, *Cataclysmic Variable Stars*. Cambridge University Press
- Woudt P. A., Warner B., Pretorius M. L., 2004, *MNRAS*, **351**, 1015
- Wynn G. A., King A. R., Horne K., 1997, *MNRAS*, **286**, 436